Check for updates

On the pivotal role of tetrel bonding in the supramolecular architectures of Pb(II)–NCS complexes with chelating thiosemicarbazide derivatives†

Bagher Eftekhari-Sis, [iD] [a] Isabel García-Santos, [iD] *[b] Alfonso Castiñeiras, [iD] [b] Ghodrat Mahmoudi, [iD] *[a] Ennio Zangrando, [iD] [c] Antonio Frontera [iD] *[d] and Damir A. Safin [iD] *[ef]

Three new Pb(II) complexes [Pb(L(I))(SCN)]$_n$, {[Pb(L(II))](SCN)}$_n$ and {[Pb(HL(III))(SCN)](SCN)}$_n$ (HL(I) = N′-phenyl(pyridin-2-yl)methylene-N-phenylthiosemicarbazide, HL(II) = N′-amino(pyrazin-2-yl)methylenethiosemicarbazide, HL(III) = N′-amino(pyridin-2-yl)methylenethiosemicarbazide) have been synthesized and characterized by spectroscopic techniques and single crystal X-ray diffraction. In all complexes, the corresponding organic ligand behaves as a tridentate N,N′,S-chelating species. A 1D supramolecular polymeric aggregation in complex [Pb(L(I))(SCN)]$_n$ is dictated by the Pb⋯NCS and Pb⋯S=C tetrel bonds formed between the [Pb(L(I))(SCN)] species. 1D cationic coordination polymers ([Pb(L(II))])$_n$$^{n+}$ in the structure of complex {[Pb(L(II))](SCN)}$_n$ are linked into a 2D supramolecular polymeric layer through the Pb⋯NCS tetrel bonds and Pb⋯π(NCS) interactions formed with the nitrogen atom and the conjugated system of the free SCN$^-$ anions, respectively. The cationic species [Pb(HL(III))(SCN)]$^+$ in the structure of complex {[Pb(HL(III))(SCN)](SCN)}$_n$ produce a 1D supramolecular polymer due to the Pb⋯SCN and Pb⋯S=C tetrel bonds, further stabilized by the Pb⋯π(NCS) interactions formed with the conjugated system of the coordinated NCS$^-$ anion. The latter anions also link these 1D chains through the Pb⋯SCN tetrel bonds, yielding 1D supramolecular polymeric ribbons. The energetic relevance of the Pb⋯S and Pb⋯N tetrel bonds has been studied by DFT calculations. The tetrel bonds have been characterized using QTAIM and NCIplot analysis and rationalized using molecular electrostatic potential surface calculations.

Introduction

Lead complexes with multidentate ligands are of significant importance in the realm of inorganic chemistry, primarily due to their unique structural and chemical properties.[1,2]

[a] Department of Chemistry, Faculty of Science, University of Maragheh, P.O. Box 55136-83111, Maragheh, Iran

[b] Departamento de Química Inorgánica, Facultad de Farmacia, Universidad de Santiago de Compostela, E-15782 Santiago de Compostela, Spain. E-mail: isabel.garcia@usc.es

[c] Department of Chemical and Pharmaceutical Sciences, University of Trieste, Via L. Giorgieri 1, 34127 Trieste, Italy

[d] Department of Chemistry, Universitat de les Illes Balears, Crta. de Valldemossa km 7.5, 07122 Palma de Mallorca (Baleares), Spain

[e] University of Tyumen, Volodarskogo Str. 6, 625003 Tyumen, Russian Federation. E-mail: damir.a.safin@gmail.com

[f] Scientific and Educational and Innovation Center for Chemical and Pharmaceutical Technologies, Ural Federal University named after the First President of Russia B.N. Yeltsin, Ekaterinburg, 620002, Russian Federation

† CCDC 2310953, 2310954 and 2324741. For crystallographic data in CIF or other electronic format see DOI: https://doi.org/10.1039/d3ce01207g

Multidentate ligands, known for their ability to coordinate to a metal atom at multiple points, play a crucial role in stabilizing lead ions in these complexes. Despite lead's status as a globally recognized toxic heavy metal pollutant,[3,4] its inherent characteristics have captivated chemists, fuelling extensive research in areas such as coordination chemistry, catalytic properties and photochemistry.[5–13] Recently, there has also been a growing interest in exploring the luminescent properties of lead-based polymers.[14,15]

The ability of polydentate ligands to form strong and specific interactions with lead ions not only enhances the stability of the complexes but also allows for precise control over their chemical and physical properties.[1–15] As a result, understanding the nature of these interactions and the resulting complexes is vital for advancing both theoretical knowledge and practical applications in chemistry.

Lead exhibits a great variety of coordination numbers[16–20] and two distinct coordination modes: hemidirectional and holodirectional.[21] In hemidirectional coordination, lead atoms display a preference for interactions on one side of

their coordination sphere, often resulting in asymmetric or incomplete geometries. This mode is indicative of lead's inclination towards softer,[22] more polarizable ligands, reflecting its unique electronic configuration and relativistic effects. On the other hand, holodirectional coordination[23] sees lead atoms engaging in more uniform and symmetrical interactions around their coordination sphere.[21] The ability of lead to toggle between these two coordination modes not only highlights its chemical versatility but also underscores the importance of considering electronic and steric factors when designing lead-containing complexes.
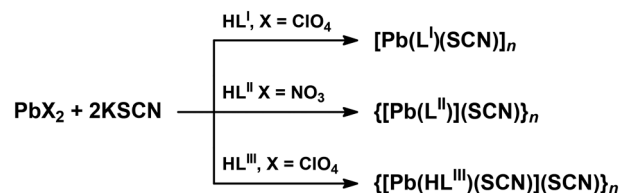
The utilization of lead in crystal engineering, particularly through the formation of Pb···O, S, N tetrel bonds, represents an interesting aspect of material science and inorganic chemistry.[24–41] Tetrel bonding, involving the interaction between a group 14 element[42,43] (like lead) and an electron rich atom (such as oxygen, sulfur or nitrogen), is pivotal in the construction of intricate crystal structures.[44] In this context, lead, with its large atomic radius and significant polarizability, forms strong and directionally specific interactions with a variety of electron donors, including π-systems.[45] These tetrel bonding interactions are instrumental in dictating the assembly and properties of crystal networks.[24–45] This approach in crystal engineering not only broadens the horizon for creating new materials but also offers deep insights into the fundamental interactions governing the assembly of complex crystal structures.

In this manuscript we report the synthesis, spectroscopic and X-ray characterization, and DFT studies of three new Pb^{II} complexes $[Pb(L^{I})(SCN)]_n$, $\{[Pb(L^{II})](SCN)\}_n$ and $\{[Pb(HL^{III})(SCN)](SCN)\}_n$ (HL^{I} = N'-phenyl(pyridin-2-yl)-methylene-N-phenylthiosemicarbazide, HL^{II} = N'-amino(pyrazin-2-yl)methylenethiosemicarbazide, HL^{III} = N'-amino(pyridin-2-yl)methylenethiosemicarbazide) (Chart 1).

Results and discussion

A reaction of an equimolar mixture of PbX_2 (X = ClO_4, NO_3) and $HL^{I–III}$ in the presence of two equivalents of KSCN leads to the formation of crystals of new supramolecular coordination structures $[Pb(L^{I})(SCN)]_n$, $\{[Pb(L^{II})](SCN)\}_n$ and $\{[Pb(HL^{III})(SCN)](SCN)\}_n$, respectively (Scheme 1).

Complexes $[Pb(L^{I})(SCN)]_n$, $\{[Pb(HL^{III})(SCN)](SCN)\}_n$ and $\{[Pb(L^{II})](SCN)\}_n$ crystallized in monoclinic $P2_1/n$ and $I2/a$, and triclinic $P\bar{1}$ space groups, respectively. The asymmetric unit of $[Pb(L^{I})(SCN)]_n$ and $\{[Pb(L^{II})](SCN)\}_n$ contains $[Pb(L^{I})(SCN)]$ and $[Pb(L^{II})](SCN)$ species, while the asymmetric unit of complex $\{[Pb(HL^{III})(SCN)](SCN)\}_n$, due to the presence

Scheme 1 Synthesis of the described complexes.

of the parent organic ligand in the neutral form, contains one cationic species $[Pb(HL^{III})(SCN)]^+$ and one SCN^- anion (Fig. 1). In all three complexes, both the deprotonated and neutral forms of the corresponding organic ligands are N,N', S-coordinated to one Pb^{II} cation with the formation of two five-membered chelate cycles (Fig. 1).

In the reported complexes, the Pb–N bonds formed with the nitrogen atom of the aromatic ring vary from 2.563(2) Å to 2.702(2) Å, with the shortest and longest values found in the structures of $\{[Pb(HL^{III})(SCN)](SCN)\}_n$ and $\{[Pb(L^{II})](SCN)\}_n$, respectively (Table 1). The Pb–N bonds formed with the imine nitrogen atom are only about 0.06 Å shorter in comparison to the corresponding bond with the pyridine nitrogen atom in the structures of $[Pb(L^{I})(SCN)]_n$ and $\{[Pb(HL^{III})(SCN)](SCN)\}_n$ (Table 1). However, the same bond is about 0.22 Å shorter in comparison to the corresponding bond with the pyrazine nitrogen atom in the structure of $\{[Pb(L^{II})](SCN)\}_n$ (Table 1). The Pb–S distance with the thiocarbonyl sulfur atom is similar in the structures of complexes and varies from 2.771(6) Å to 2.8539(9) Å (Table 1).

In the structure of $[Pb(L^{I})(SCN)]_n$, the coordination sphere of the Pb^{II} cation is filled by the sulfur atom of the covalently bound SCN^- anion, further completed by tetrel bound two thiocyanate nitrogen and two thiocarbonyl sulfur atoms from two adjacent $[Pb(L^{I})(SCN)]$ molecules (Fig. 1 and 2, Table 1). Thus, the overall coordination geometry of the Pb^{II} cation in $[Pb(L^{I})(SCN)]_n$ is described as a N_4S_4 eight-membered environment. The covalent Pb–S and tetrel Pb···S bonds formed with the thiocarbonyl sulfur atoms of the ligands L^{I} are responsible for the formation of the Pb_2S_2 coordination cores of the parallelogram type with the Pb···Pb separations of 4.575(2) Å and 4.218(2) Å (Fig. 3, Table 1). These Pb_2S_2 cores form a central backbone of the 1D supramolecular polymeric chain of $[Pb(L^{I})(SCN)]_n$, which, in turn, is further stabilized by N4–H4A···N5 hydrogen bonds formed between the NH hydrogen atom and the thiocyanate nitrogen atom (Fig. 3, Table 2). Furthermore, both sides of the Pb_2S_2 cores, constructed from two covalent Pb–S and two tetrel Pb···S bonds, are involed in the interaction with the thiocyanate C1–N5 fragments (Fig. 3, Table 2). Finally, 1D supramolecular polymeric chains are linked through the C4–H4···Ph_{C9} interactions (Table 2), yielding an extended 3D supramolecular framework.

In the structure of $\{[Pb(L^{II})](SCN)\}_n$, the coordination sphere of the Pb^{II} cation also includes one amide nitrogen and one thiocarbonyl sulfur atoms from two adjacent cationic species $[Pb(L^{II})]^+$ (Fig. 2, Table 1). The overall
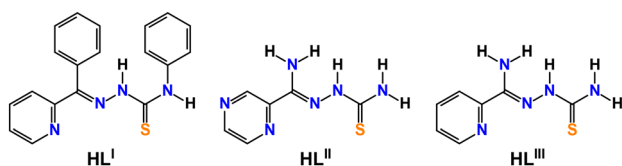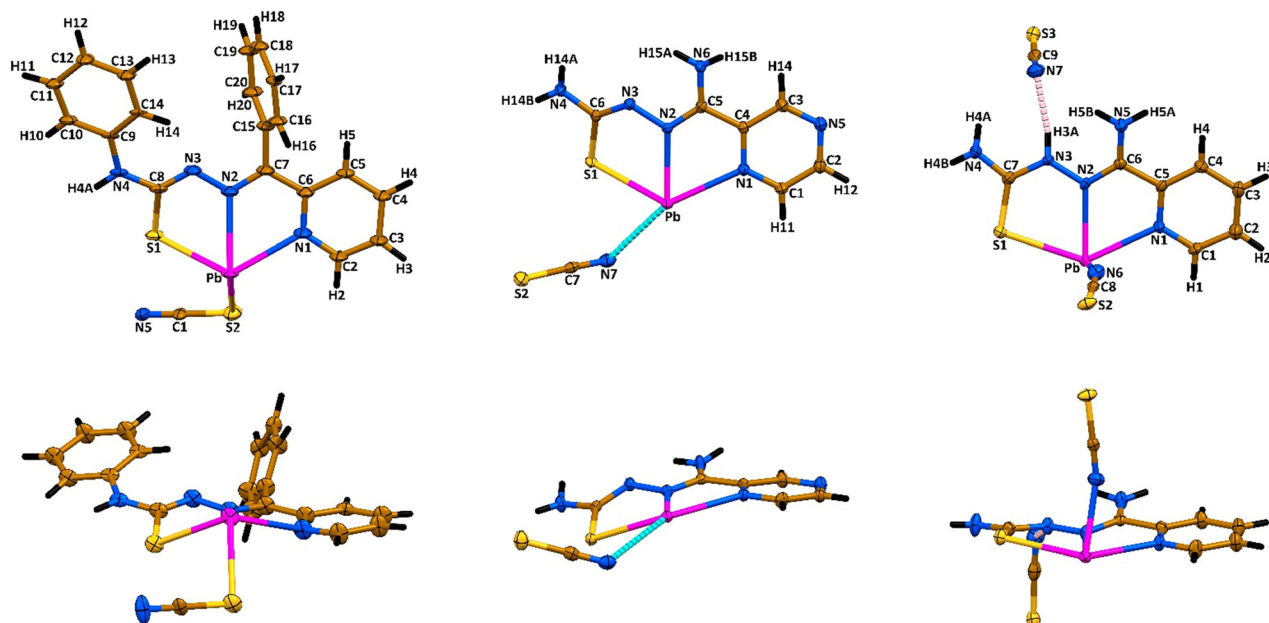
Chart 1 Thiosemicrbazide derivatives used as ligands in this work.

Fig. 1 Top and side views on the asymmetric units of [Pb(L^I)(SCN)]$_n$ (left), {[Pb(L^{II})](SCN)}$_n$ (middle) and {[Pb(HL^{III})(SCN)](SCN)}$_n$ (right). Displacement ellipsoids are drawn with the 50% probability. Color code: H = black, C = gold, N = blue, S = yellow, Pb = magenta; Pb···N tetrel bond = cyan dashed line, N–H···N hydrogen bond = pink dashed line.

Table 1 Selected bond lengths (Å) in the crystal structures of the described complexes (see Fig. 1 for atoms labelling)

Bond	Bond length	Bond type	Bond	Bond length	Bond type
[Pb(L^I)(SCN)]$_n$^{a}					
Pb–N1	2.63(2)	Covalent	Pb···S1$^{\#2}$	3.123(6)	Tetrel
Pb–N2	2.57(2)	Covalent	Pb···N5$^{\#1}$	3.26(2)	Tetrel
Pb–S1	2.771(6)	Covalent	Pb···N5$^{\#2}$	3.25(2)	Tetrel
Pb–S2	2.949(7)	Covalent	Pb···Pb$^{\#2}$	4.575(2)	
Pb···S1$^{\#1}$	3.213(6)	Tetrel	Pb···Pb$^{\#3}$	4.218(2)	
{[Pb(L^{II})](SCN)}$_n$^{b}					
Pb–N1	2.702(2)	Covalent	Pb···N7	2.922(2)	Tetrel
Pb–N2	2.484(2)	Covalent	Pb···π(NCS)$^{\#3}$	3.338	Tetrel
Pb–N3$^{\#1}$	2.780(2)	Covalent	Pb···Pb$^{\#1}$	4.9682(4)	
Pb–S1	2.7982(7)	Covalent	Pb···Pb$^{\#2}$	4.1220(4)	
Pb–S1$^{\#2}$	2.9196(7)	Covalent			
{[Pb(HL^{III})(SCN)](SCN)}$_n$^{c}					
Pb–N1	2.563(2)	Covalent	Pb···S2$^{\#2}$	3.5182(9)	Tetrel
Pb–N2	2.500(3)	Covalent	Pb···S2$^{\#3}$	3.3687(10)	Tetrel
Pb–N6	2.460(3)	Covalent	Pb···π(NCS)$^{\#1}$	3.254	Tetrel
Pb–S1	2.8539(9)	Covalent	Pb···Pb$^{\#1}$	4.5552(4)	
Pb···S1$^{\#1}$	3.1455(9)	Tetrel	Pb···Pb$^{\#4}$	4.5552(4)	

^{a} Symmetry codes: #1 1 + x, y, z; #2 1 − x, 1 − y, 1 − z; #3 2 − x, 1 − y, 1 − z. ^{b} Symmetry codes: #1 1 − x, 1 − y, 1 − z; #2 −x, 1 − y, 1 − z; #3 −x, −y, 1 − z. ^{c} Symmetry codes: #1 1/2 + x, 1 − y, z; #2 1 + x, y, z; #3 1/2 − x, y, −z; #4 −1/2 + x, 1 − y, z.

coordination geometry of the Pb^{II} cation in {[Pb(L^{II})](SCN)}$_n$ is described as a N$_4$S$_2$(NCS) environment. Besides the covalent Pb–N and Pb–S bonds, the coordination sphere of the metal cation is completed by one Pb···N tetrel bond with the nitrogen atom of the free NCS$^−$ anion and the π-system of the other free NCS$^−$ anion (Fig. 2, Table 1). Aggregation of the [Pb(L^{II})]$^+$ cations yields a 1D supramolecular cationic polymeric chain [Pb(L^{II})]$_n$$^{n+}$, which central backbone is

constructed from the Pb$_2$S$_2$ parallelograms and Pb$_2$N$_4$ cycles of the chair conformation with the Pb···Pb separations of 4.1220(4) Å and 4.9682(4) Å, respectively (Fig. 2, Table 1). The 1D supramolecular cationic polymeric chains [Pb(L^{II})]$_n$$^{n+}$ are linked into a 2D supramolecular layer through the Pb···N and Pb···π(NCS) tetrel bonds formed with the interchain thiocyanate anions (Fig. 3, Table 1), and N4–H14A···S2 and N6–H15A···N7 hydrogen bonds formed between the sulfur
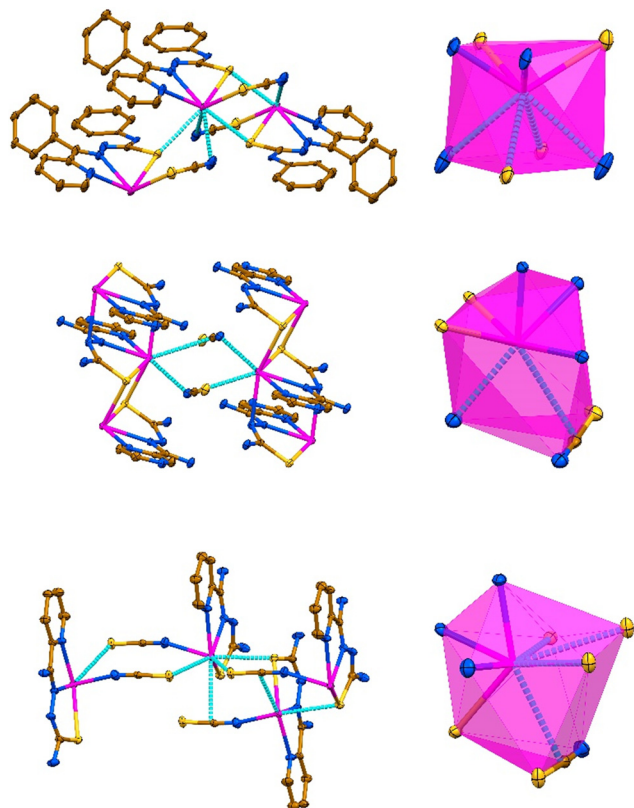
Fig. 2 Supramolecular aggregation together with the corresponding coordination polyhedra in the crystal structures of [Pb(L^I)(SCN)]$_n$ (top), {[Pb(L^{II})](SCN)}$_n$ (middle) and {[Pb(HL^{III})(SCN)](SCN)}$_n$ (bottom). Displacement ellipsoids are drawn with the 50% probability. Hydrogen atoms were omitted for clarity. Color code: C = gold, N = blue, S = yellow, Pb = magenta; Pb⋯N, Pb⋯S and Pb⋯π(NCS) tetrel bonds = cyan dashed line.

Fig. 3 1D supramolecular polymeric chains in the crystal structures of [Pb(L^I)(SCN)]$_n$ (top) and {[Pb(HL^{III})(SCN)](SCN)}$_n$ (bottom), and a 2D supramolecular layer in the structure of {[Pb(L^{II})](SCN)}$_n$ (middle). Displacement ellipsoids are drawn with the 50% probability. Hydrogen atoms were omitted for clarity. Color code: C = gold, N = blue, S = yellow, Pb = magenta; Pb⋯N, Pb⋯S and Pb⋯π(NCS) tetrel bonds = cyan dashed line.

and nitrogen atoms of the same thiocyanate anions and hydrogen atoms of two NH$_2$ groups of the organic ligand **L^{II}** (Fig. 2, Table 2). Furthermore, the C1–H11⋯S2 interactions between the thiocyanate sulfur atoms and one of the pyrazine hydrogen atoms stabilize these layers (Table 2). The resulting 2D supramolecular layers are linked into a 3D supramolecular framework through the N4–H14B⋯N5 hydrogen bonds, formed between the second hydrogen atom of the NH$_2$ group attached to the thiocarbonyl fragment and the free pyrazine nitrogen atom (Table 2). The resulting supramolecular 3D framework is further reinforced by π⋯π interactions between the pyrazine cycles (Table 2).

In the crystal structure of {[Pb(HL^{III})(SCN)](SCN)}$_n$, the coordination sphere of the Pb^{II} cation, besides a covalently linked tridentate **HL^{III}** ligand and a monodentate N-bound thiocyanate anion, is described by the formation of three Pb⋯S tetrel bonds with one thiocarbonyl and two thiocyanate sulfur atoms from three adjacent cationic species [Pb(HL^{III})(SCN)]$^+$ (Fig. 2, Table 1). Notably, the thiocyanate ligand of the adjacent [Pb(HL^{III})(SCN)]$^+$ cation, which thiocarbonyl sulfur atom forms a Pb⋯S tetrel bond, further completes the coordination sphere of the Pb^{II} cation by the Pb⋯π(NCS) tetrel bond (Fig. 2, Table 1). Thus, the

coordination sphere of metal cation is described as a N$_3$S$_4$(NCS) environment. Tetrel bonds in the structure of {[Pb(HL^{III})(SCN)](SCN)}$_n$ are responsible for the formation of a 1D supramolecular polymeric chain [Pb(HL^{III})(SCN)]$_n^{n+}$ (Fig. 3), with the shortest Pb⋯Pb separations of 4.5552(4) Å (Table 1). These supramolecular chains are separated by the noncoordinated thiocyanate anions, which, in turn, are linked through the N–H⋯N and N–H⋯S hydrogen bonds with the NH and NH$_2$ hydrogen atoms of the organic ligands

Table 2 Hydrogen bond and other noncovalent, and π⋯π interaction lengths (Å) and angles (°) in the crystal structures of the described complexes (see Fig. 1 for atoms labelling)

D–X⋯A	d(D–X)	d(X⋯A)	d(D⋯A)	∠(DXA)
$[Pb(L^{I})(SCN)]_n$ [a]				
N4–H4A⋯N5#1	0.88	2.18	3.06(3)	171
C4–H4⋯Ph$_{Cg}$#2	0.95	2.82	3.58(3)	137
C1–N5⋯Pb$_2$S1$_2$	1.16(3)	2.94(2)	2.90(2)	76.7(16)
C1–N5⋯Pb$_2$S1$_2$#1	1.16(3)	2.94(2)	2.90(2)	76.7(16)
$\{[Pb(L^{II})](SCN)\}_n$ [b]				
N4–H14A⋯S2#1	0.92	2.69	3.571(2)	162
N4–H14B⋯N5#2	0.80	2.23	3.023(3)	175
N6–H15A⋯N7#1	0.86	2.22	3.008(3)	154
C1–H11⋯S2#3	0.93	2.86	3.631(2)	141
$\{[Pb(HL^{III})(SCN)](SCN)\}_n$ [c]				
N3–H3A⋯N7#1	0.85	1.98	2.817(4)	168
N4–H4A⋯S3#2	0.80	2.84	3.404(3)	130
N4–H4A⋯N7#1	0.80	2.51	3.153(5)	139
N4–H4B⋯S3#3	0.78	2.61	3.364(3)	163
N5–H5A⋯S3#4	0.89	2.53	3.411(3)	168
N5–H5B⋯N7#5	0.87	2.46	3.103(4)	131
C4–H4⋯S3#4	0.95	2.72	3.652(3)	167

Cg(*I*)	Cg(*J*)	d[Cg(*I*)⋯Cg(*J*)]	α	β	γ	Slippage
$\{[Pb(L^{II})](SCN)\}_n$ [b]						
Pyrz	Pyrz#4	3.8962(15)	0.00(14)	30.4	30.4	1.970
$\{[Pb(HL^{III})(SCN)](SCN)\}_n$ [c]						
Py	Py#4	4.019(2)	5.61(17)	29.1	26.2	1.955
Py	Py#6	4.019(2)	5.61(17)	26.2	29.1	1.775

[a] Symmetry codes: #1 $-x$, $1 - y$, $1 - z$; #2 $3/2 - x$, $-1/2 + y$, $1/2 - z$; [b] Symmetry codes: #1 $1 + x$, $1 + y$, z; #2 x, y, $1 + z$; #3 $-x$, $-y$, $1 - z$; #4 $1 - x$, $1 - y$, $-z$. [c] Symmetry codes: #1 $3/2 - x$, $1/2 - y$, $1/2 - z$; #2 $1 - x$, $1/2 + y$, $1/2 - z$; #3 $-1/2 + x$, $1 - y$, z; #4 $-1/2 + x$, $-y$, z; #5 $-1 + x$, y, z; #6 $-1/2 + x$, $-y$, z.

HL^{III} (Table 2). Furthermore, one of the pyridine hydrogen atoms is also involved in the C–H⋯S interaction with the noncoordinated thiocyanate anion (Table 2). Finally, 1D supramolecular chains are interlinked through π⋯π interactions between the pyridine cycles (Table 2).

All the obtained complexes were further studied by ^{1}H NMR spectroscopy in DMSO-d_6 and compared with those of the corresponding parent ligands in the same solvent. Notably, the spectrum of HL^I exhibits two sets of signals corresponding to the *E*- and *Z*-isomers, of which the latter one is dominant in solution of DMSO-d_6 (Fig. 4). The spectra of $[Pb(L^I)(SCN)]_n$ and $\{[Pb(L^{II})](SCN)\}_n$ contain a single set of peaks, which were observed in the regions typical for protons of the certain nature (phenyl, pyridine and pyrazine fragments; NH and NH$_2$ groups) (Fig. 4). Interestingly, the ^{1}H NMR spectrum of $\{[Pb(HL^{III})(SCN)](SCN)\}_n$ in the same solvent exhibits two sets of peaks with a ratio of about 1 : 4 (Fig. 4). The minor set of peaks was attributed to the $[Pb(HL^{III})(SCN)](SCN)$ species, while the major set of peaks was tentatively assigned to the $[Pb(L^{III})(SCN)]$ species. Thus, in

DMSO-d_6, complex $\{[Pb(HL^{III})(SCN)](SCN)\}_n$ exhibits the following equilibrium: $[Pb(HL^{III})(SCN)](SCN) \leftrightarrow [Pb(L^{III})(SCN)] + HSCN$. We can tentatively explain this equilibrium by the formation of strong intermolecular hydrogen bond N3–H3A⋯N7 formed between the NH hydrogen atom of the organic ligand HL^{III} and the nitrogen atom of the free thiocyanate anion (Fig. 1, Table 2), which allows to withdraw the corresponding hydrogen atom.

This study concentrates on examining the intriguing tetrel bonding interactions that facilitate the formation of the reported supramolecular polymers. Initially, the molecular electrostatic potential (MEP) surfaces of complexes $[Pb(L^I)(SCN)]$ and $[Pb(HL^{III})(SCN)](SCN)$ were calculated to explore the presence and intensity of σ-holes at the Pb^{II} centers. The MEP surfaces reveal that the MEP maximum is situated at the Pb^{II} center in $[Pb(L^I)(SCN)]$ and at the amino group of the cationic $[Pb(HL^{III})(SCN)]^+$ species in $[Pb(HL^{III})(SCN)](SCN)$ (Fig. 5). Detailed analysis of the MEP at the Pb^{II} center in $[Pb(L^I)(SCN)]$ indicates the existence of three σ-holes, suggesting directional characteristics for the tetrel bonds involving the hemicoordinated Pb^{II} cation. Notably, the MEP values at the σ-holes in $[Pb(HL^{III})(SCN)](SCN)$, ranging from 51 to 60 kcal mol^{-1}, are higher than those in $[Pb(L^I)(SCN)]$ (26 to 33 kcal mol^{-1}), which can be attributed to the ion-pair nature of the former complex. The MEP minima are located at the thiocyanate anion, with $[Pb(L^I)(SCN)]$ showing a significantly less negative value (-57 kcal mol^{-1} at the nitrogen atom) compared to $[Pb(HL^{III})(SCN)](SCN)$ (-68 kcal mol^{-1}), a result of the non-coordination of the anion. The MEP values are positive over the π-system of the coordinated pyridine fragment in both compounds, recorded at 19 and 39 kcal mol^{-1} in $[Pb(L^I)(SCN)]$ and $[Pb(HL^{III})(SCN)](SCN)$, respectively (Fig. 5). Conversely, the MEP is negative over the phenyl group in $[Pb(L^I)(SCN)]$, measuring -13 kcal mol^{-1}.

We have also applied the quantum theory of atoms in molecules (QTAIM) in conjunction with the non-covalent interaction (NCI) plot to more comprehensively characterize the tetrel bonds in the discussed complexes. This dual approach effectively reveals interactions in real space. Furthermore, the colour coding of the reduced density gradient (RDG) isosurfaces assists in distinguishing between attractive and repulsive interactions, with green indicating weak noncovalent interactions and blue denoting strong ones.

We have also focused specifically on the QTAIM/NCI plot characterization of tetrel bonds for two dimers of complex $[Pb(L^I)(SCN)]_n$ (Fig. 6). The QTAIM analysis identified two symmetrically equivalent Pb⋯S contacts, each marked by a bond critical point (CP), depicted as a small red sphere, and a bond path, illustrated as a dashed bond, linking the atoms the centrosymmetric dimer (Fig. 6, left). Additionally, this analysis revealed the presence of two Pb⋯N interactions, with corresponding bond CPs and paths connecting the Pb^{II} centers to the terminal nitrogen atom of the thiocyanate ligand. In this dimer, the NCI plot analysis displays blue isosurfaces between the Pb^{II} and sulfur atoms, coinciding
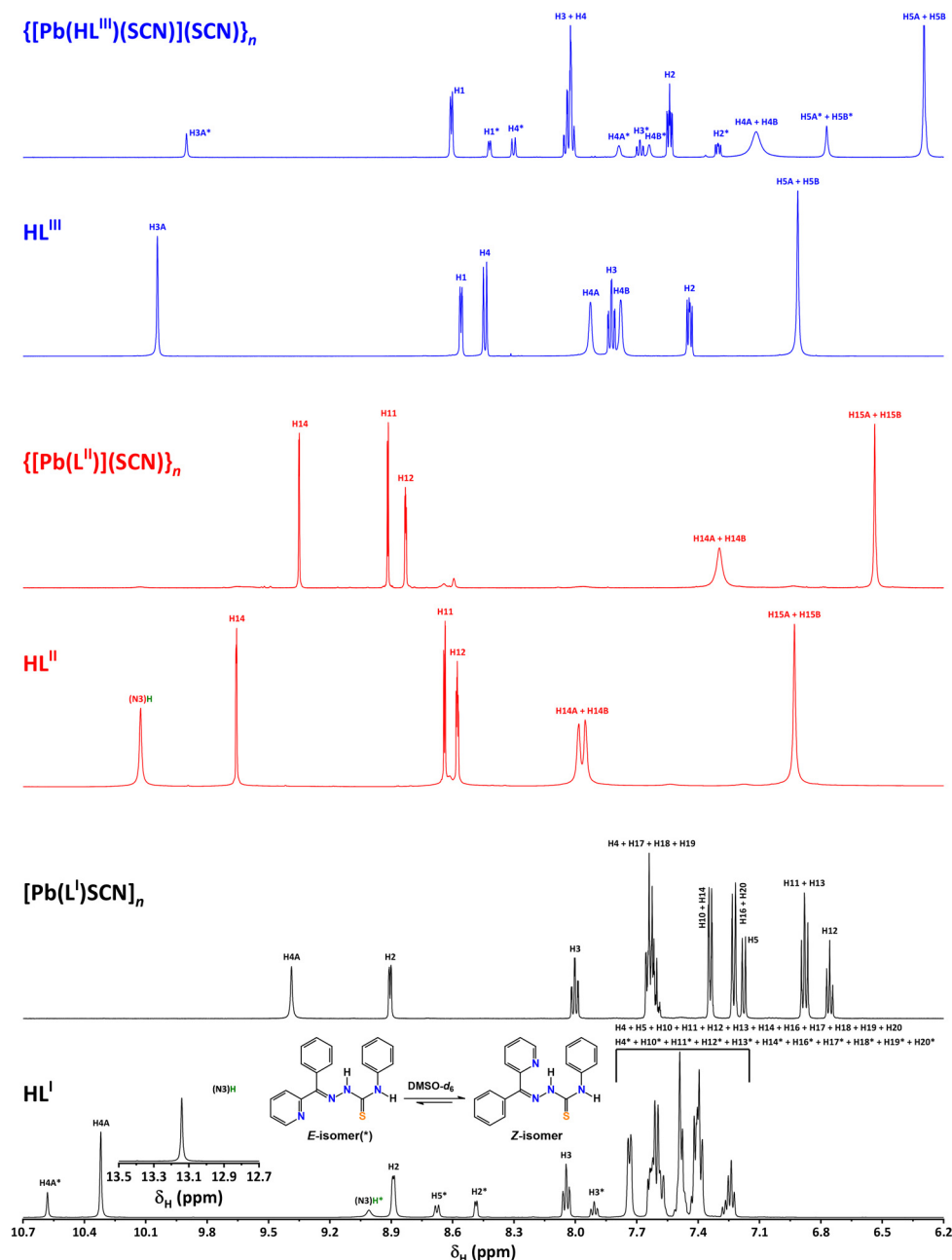
Fig. 4 The ^{1}H NMR spectra of HL$^{I–III}$, [Pb(L^I)(SCN)]$_n$, {[Pb(L^{II})](SCN)}$_n$ and {[Pb(HL^{III})](SCN)](SCN)}$_n$ recorded in DMSO-d_6 (see Fig. 1 for peak labelling).

with the bond CPs, and green isosurfaces for the Pb···N tetrel bonds, indicating that the Pb···S tetrel bonds are stronger than the secondary Pb···N bonds. This arrangement aligns with the MEP analysis, which shows electron-rich sulfur and nitrogen atoms positioned at the σ-holes. Consequently, the large dimerization energy of this dimer (−35.5 kcal mol$^{−1}$) is attributed to the formation of four concurrent and electrostatically enhanced tetrel bonds.

In the other dimer, extracted from the solid-state structure of [Pb(L^I)(SCN)]$_n$, the Pb^{II} cation forms two tetrel bonds with the sulfur and nitrogen atoms of the adjacent molecule, each characterized by a bond CP, bond path and a green-bluish

RDG isosurface (Fig. 6, right). Moreover, three additional bond CPs interconnect both molecules, indicative of the C–H···π and C–H···N interactions. The dimerization energy of this assembly is lower than that of the centrosymmetric dimer (−21.2 kcal mol$^{−1}$), owing to the presence of only two tetrel bonds.

At this point, it is interesting to differentiate the coordination bonds from tetrel bonds. Using the dimer of [Pb(L^I)(SCN)]$_n$ represented in Fig. 6a as example, we have compared the values of density (ρ), its Laplacian ($\nabla^2\rho$), the potential energy density (V), the Lagrangian kinetic energy (G) and the total energy density (H). The values gathered in
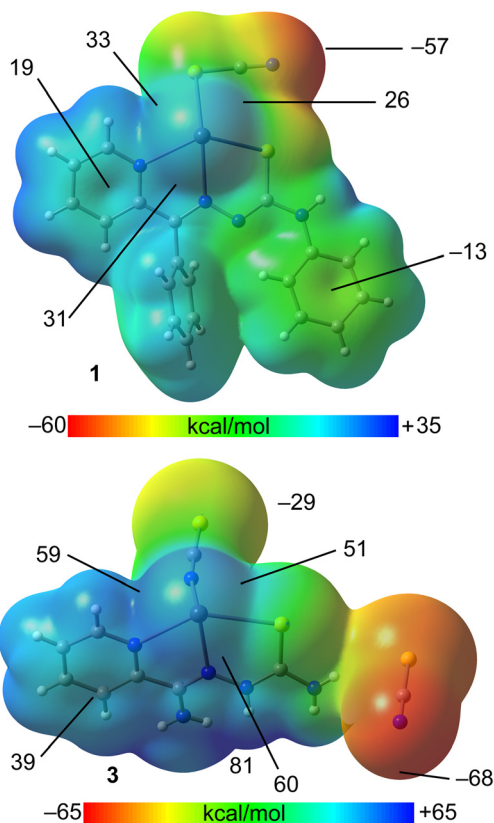
Fig. 5 MEP surfaces of [Pb(L^I)(SCN)] (top) and [Pb(HL^III)(SCN)](SCN) (bottom) using a 0.001 a.u. isodensity.

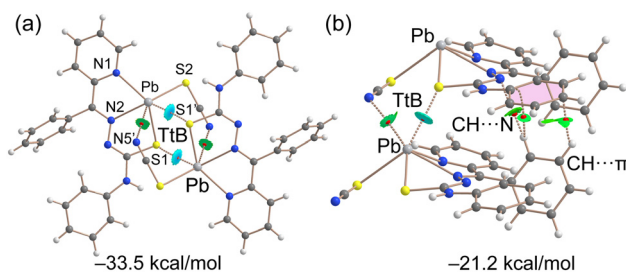**Fig. 6** (a) QTAIM/NCI plot analysis of a dimer of [Pb(L^I)(SCN)]$_n$, where only the tetrel bonds are indicated. (b) QTAIM/NCI plot analysis of a dimer of [Pb(L^I)(SCN)]$_n$, where tetrel bonds, hydrogen bonds and C–H···π interactions are indicated.

Table 3 are measured at the bond CPs that characterize both the tetrel and coordination bonds, represented by dashed and solid bonds in Fig. 6, respectively.

The values of density at the bond CPs that characterize the coordination bonds are in all cases greater than 0.035 a.u. whilst those of the tetrel bonds are smaller than 0.024 a.u., in the range of typical noncovalent interactions.[28–31] Similarly, the values of $\nabla^2\rho$ are larger for the coordination bonds than for the Pb···S1′ and Pb···N5′ tetrel bonds. A convenient criterion to differentiate coordination (partial covalent character) from tetrel bonds (non covalent) is the total energy density ($H = V + G$) since it has been previously demonstrated that negative

Table 3 Electron charge density (ρ), its Laplacian ($\nabla^2\rho$), kinetic (V), Lagrangian (G) and total (H) energy densities at the bond critical points (CPs) that characterize both coordination and tetrel bonds in the dimer of [Pb(L^I)(SCN)]$_n$ shown in Fig. 6a

Bond	ρ	$\nabla^2\rho$	V	G	H
Pb–N1	0.0393	0.0989	−0.0320	0.0284	−0.0036
Pb–N2	0.0433	0.1101	−0.0371	0.0323	−0.0048
Pb–S1	0.0487	0.1699	−0.0358	0.0267	−0.0091
Pb–S2	0.0353	0.0726	−0.0220	0.0176	−0.0044
Pb···S1′	0.0105	0.0296	−0.0138	0.0138	0.0000
Pb···N5′	0.0239	0.0482	−0.0052	0.0063	0.0011

values of H are an indication of covalency.[46] Remarkably the values of H are negative for the coordination bonds, ranging from $−3.6 \times 10^{−3}$ a.u to $−9.1 \times 10^{−3}$ and those of Pb···S1′ and Pb···N5′ tetrel bonds are positive or negligible, confirming the ability of QTAIM parameters to differentiate coordination and tetrel bonding interactions.

We extended our computational studies to complex {[Pb(HL^III)(SCN)](SCN)}$_n$ (Fig. 7), utilizing a dimer extracted from the corresponding supramolecular polymer, for both energetic and QTAIM/NCI plot analyses. For the energy calculations, each ion pair was treated as an individual monomer. The dimerization energy of −28.2 kcal mol$^{−1}$ is comparable to that observed in the dimers of [Pb(L^I)(SCN)]$_n$, highlighting the energetic significance of tetrel bonds in the solid state. The QTAIM/NCI plot analysis reveals that the noncoordinated thiocyanate anion forms a trifurcated hydrogen bond with the [Pb(HL^III)(SCN)]$^+$ cation (Fig. 7), aligning with the MEP maximum (Fig. 5). The strongest hydrogen bond, indicated by the most intense blue RDG isosurface, occurs with the hydrocarbazide NH group. Dimerization of each ion pair is facilitated by two Pb···S bonds, each characterized by a corresponding bond CP, bond path and blue RDG isosurface.

Intriguingly, the QTAIM/NCI plot analysis also uncovers the formation of antiparallel C–N···C–N interactions between the coordinated thiocyanate groups (Fig. 7). This interaction is characterized by a bond CP and bond path linking the CN groups, along with a green and extended RDG isosurface situated between the thiocyanate ligands. The relevance of such antiparallel C–N···C–N interactions in crystal engineering has been previously established.[47,48]
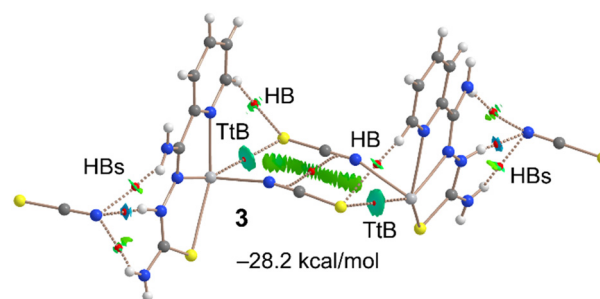
Fig. 7 QTAIM/NCI plot analysis of dimer of {[Pb(HL^III)(SCN)](SCN)}$_n$, where only intermolecular interactions are indicated.

Concluding remarks

In this study, we present the synthesis and structural characterization of three new Pb^{II} complexes, incorporating thiocyanate anions and various thiosemicarbazide derived ligands. The Pb^{II} centers exhibit hemidirected coordination, which is key to enabling σ-hole interactions. These interactions play a pivotal role in the self-assembly of dimers and their further extension into polymeric structures. Additionally, our DFT theoretical calculations highlight the energetic significance of these tetrel bonds.

The complexes presented in this study represent advancements in the field of crystal engineering and coordination chemistry, particularly concerning lead-based supramolecular assemblies. Their structural properties, mostly derived from tetrel bonding interactions, open up possibilities for application in areas like material science, where they could be explored for their potential use in designing new materials with specific electronic or optical properties. Moreover, the insights gained into the nature of tetrel bonds can aid in the development of lead-based catalysts or sensors. Future research could focus on exploring these applications in more detail.

Experimental

Materials and physical measurements

All the reagents and solvents were commercially available and used without further purification. HL^{I-III} were prepared as reported.[24] The FTIR spectra in the KBr pellets were obtained with a FT 801 spectrometer. The ^1H NMR spectra in DMSO-d_6 were recorded with a Bruker DPX NMR-400 spectrometer. Microanalyses were performed using a LECO-elemental analyzer.

Synthesis

$[Pb(L^I)(SCN)]_n$. A suspension of $Pb(ClO_4)_2 \cdot 3H_2O$ (0.038 g, 0.082 mmol) and KSCN (0.016 g, 0.16 mmol) in water (2 mL) was added to a solution of HL^I (0.027 g, 0.082 mmol) in EtOH/CH_3CN (30 mL, 1:1). The resulting mixture was stirred for 0.5 h under reflux followed by filtration. After several days, single crystals were formed. M.p. 190 °C. Anal. calc. for $C_{20}H_{15}N_5PbS_2$ (596.69): C 40.26, H 2.53 and N 11.74%; found: C 40.10, H 4.44 and N 11.54%.

$\{[Pb(L^{II})](SCN)\}_n$. A suspension of $Pb(NO_3)_2$ (0.042 g, 0.127 mmol) and KSCN (0.024 g, 0.25 mmol) in water (2 mL) was added to a solution of HL^{II} (0.025 g, 0.127 mmol) in MeOH (30 mL). The resulting mixture was stirred for 0.5 h under reflux followed by filtration. After several days, single crystals were formed. M.p. 245 °C. Anal. calc. for $C_7H_7N_7PbS_2$ (460.50): C 18.26, H 1.53 and N 21.29%; found: C 18.20, H 1.52 and N 21.36%.

$\{[Pb(HL^{III})(SCN)](SCN)\}_n$. A suspension of $Pb(ClO_4)_2 \cdot 3H_2O$ (0.060 g, 0.13 mmol) and KSCN (0.025 g, 0.26 mmol) in water (2 mL) was added to a solution of HL^{III} (0.025 g, 0.13 mmol) in MeOH (30 mL). The resulting mixture was stirred for 0.5 h under reflux followed by filtration. After several days, single crystals were formed. M.p. 210 °C. Anal. calc. for $C_9H_9N_7PbS_3$ (518.60): C 20.84, H 1.75 and N 18.91%; found: C 20.81, H 1.65 and N 18.83%.

Single-crystal X-ray diffraction

Single crystals of complexes were mounted on a glass fiber and diffraction data were collected at 100(2) K on a Bruker D8 Venture Photon III-14 diffractometer using graphite monochromated Mo-Kα radiation (λ = 0.71073 Å). Data reductions were performed with APEX3 software package[49] and proper absorption corrections were applied to the data sets.[50] The structures were solved by direct methods with SHELXS-2013[51] and refined by full matrix least-squares procedures using the SHELXTL.[51] The hydrogen atoms were placed at calculated positions and constrained to ride to atoms to which they are attached, except those of amine groups of $\{[Pb(L^{II})](SCN)\}_n$ that were located on the Fourier map and freely refined.

The diffraction pattern of $[Pb(L^I)(SCN)]_n$ appears twinned with slightly curved shapes of spots, as if the needle-shaped crystal flexed during data collection. The data have been processed to a resolution of 0.835 Å without taking into account the contribution of the multiple minority domains of the twin, using only the orientation matrix of the main domain.

Crystal data for $[Pb(L^I)(SCN)]_n$. $C_{20}H_{15}N_5PbS_2$, M_r = 596.68 g mol^{-1}, monoclinic, space group $P2_1/n$, a = 5.6513(12), b = 19.384(4), c = 18.237(4) Å, β = 98.331(8)°, V = 1976.7(7) Å^3, Z = 4, ρ = 2.005 g cm^{-3}, μ(Mo-Kα) = 8.762 mm^{-1}, reflections: 29 693 collected, 3558 unique, R_{int} = 0.1483, R_1(all) = 0.1215, wR_2(all) = 0.2653, S = 1.231.

Crystal data for $\{[Pb(L^{II})](SCN)\}_n$. $C_7H_7N_7PbS_2$, M_r = 460.51 g mol^{-1}, triclinic, space group $P\bar{1}$, a = 6.9411(4), b = 8.1607(5), c = 10.8395(7) Å, α = 97.201(3), β = 93.084(2), γ = 107.496(2)°, V = 578.25(6) Å^3, Z = 2, ρ = 2.645 g cm^{-3}, μ(Mo-Kα) = 14.937 mm^{-1}, reflections: 69 028 collected, 4430 unique, R_{int} = 0.0740, R_1(all) = 0.0206, wR_2(all) = 0.0313, S = 1.054.

Crystal data for $\{[Pb(HL^{III})(SCN)](SCN)\}_n$. $C_9H_9N_7PbS_3$, M_r = 518.60 g mol^{-1}, monoclinic, space group $I2/a$, a = 7.8039(4), b = 11.1545(7), c = 33.709(2) Å, β = 90.944(2)°, V = 2933.9(3) Å^3, Z = 8, ρ = 2.348 g cm^{-3}, μ(Mo-Kα) = 11.927 mm^{-1}, reflections: 41 141 collected, 4472 unique, R_{int} = 0.0471, R_1(all) = 0.0224, wR_2(all) = 0.0464, S = 1.018.

DFT analysis

For the DFT calculations of the supramolecular assemblies we have used the PBE0-D3/def2-TZVP level of theory[52–54] and the Gaussian-16 program.[55] The binding energies were computed as the difference between the energy of the assembly and the sum of the isolated monomers. The energies have been corrected for the basis set superposition error.[56] The MEP surfaces were generated using the 0.001 isosurface to emulate the van der Waals envelop. The QTAIM[57] and NCI plot[58] analyses were performed and

represented at the same level using the AIMAll program.[59] The NCI plot method[58] is convenient to reveal interactions in real space. It uses the reduced density gradient isosurfaces and a colour code (based on the sign of the second eigenvalue of ρ, λ_2) to identify the attractive or repulsive nature of the interactions. Blue and green colours are used here to identify strongly and moderately attractive interactions, respectively.

Conflicts of interest

There are no conflicts to declare.

Acknowledgements

References

1 M. Kowalik, J. Masternak, K. Kazimierczuk, O. V. Khavryuchenko, B. Kupcewicz and B. Barszcz, *J. Solid State Chem.*, 2019, **273**, 207–218.

2 D.-S. Liu, L.-H. Dai, F.-Q. Qiu, D.-Z. Xi, Y. Luo, N.-N. Pi and Y. Sui, *J. Solid State Chem.*, 2021, **303**, 122540.

3 J. N. RauchJ and M. Pacyna, *Global Biogeochem. Cycles*, 2009, **23**, 16–18.

4 S. K. Marx, S. Rashid and N. Stromsoe, *Environ. Pollut.*, 2016, **213**, 283–298.

5 W. C. D. Gruijter and T. Bokx, *J. Solid State Chem.*, 1973, **6**, 271–279.

6 S. K. Dutta and M. W. Perkovic, *Inorg. Chem.*, 2002, **41**, 6938–6940.

7 E. Irran, T. Bein and N. Stock, *J. Solid State Chem.*, 2003, **173**, 293–298.

8 Z.-M. Sun, J.-G. Mao, Y.-Q. Sun, H.-Y. Zeng and A. Clearfield, *New J. Chem.*, 2003, **27**, 1326–1330.

9 J.-L. Song, C. Lei, Y.-Q. Sun and J.-G. Mao, *J. Solid State Chem.*, 2004, **177**, 2557–2564.

10 Q. Y. Liu and L. Xu, *Eur. J. Inorg. Chem.*, 2006, **8**, 1620–1628.

11 A. M. P. Peedikakkal, H. S. Quah, S. Chia, A. S. Jalilov, A. R. Shaikh, H. A. Al-Mohsin, K. Yadava, W. Ji and J. J. Vittal, *Inorg. Chem.*, 2018, **57**, 11341–11348.

12 J. Ni, S.-W. Wang, P.-P. Zhang, J.-J. Zhang, H. Zhao, E.-P. Tan, Z.-Y. Li, J. Chen and C. Xia, *Cryst. Growth Des.*, 2021, **21**, 207–217.

13 X.-S. Wu, R. Zhang and J.-L. Liu, *J. Solid State Chem.*, 2021, **301**, 122298.

14 D.-S. Liu, Z.-J. Qiu, X. Fu, Y.-Z. Liu, P. Ding, Y.-X. Zhu and Y. Sui, *J. Solid State Chem.*, 2019, **278**, 120879–120886.

15 D.-S. Liu, Z.-J. Qiu, Y.-L. Xiao, Y.-J. Shen, Q. Zhou, W.-T. Chen and Y. Sui, *J. Solid State Chem.*, 2019, **279**, 120952–120957.

16 J. Parr, *Polyhedron*, 1997, **16**, 551–566.

17 C. E. Holloway and M. Melnik, *Main Group Met. Chem.*, 1997, **20**, 399–495.

18 R. L. Davidovich, V. Stavila and K. H. Whitmire, *Coord. Chem. Rev.*, 2010, **254**, 2193–2226.

19 J. Parr, *Germanium, Tin, and Lead, Comprehensive Coordination Chemistry II*, Elsevier, Oxford, 2004, vol. 3, p. 545.

20 S. Hino, M. Brynda, A. D. Phillips and P. P. Powe, *Angew. Chem., Int. Ed.*, 2004, **43**, 2655–2658.

21 M. Imran, A. Mix, B. Neumann, H.-G. Stammler, U. Monkowius, P. Gründlinger and N. W. Mitzel, *Dalton Trans.*, 2015, **44**, 924–937.

22 R. D. Hancock and A. E. Martell, *Chem. Rev.*, 1989, **89**, 1875–1914.

23 L. Shimoni-Livny, J. P. Glusker and C. W. Bock, *Inorg. Chem.*, 1998, **37**, 1853–1867.

24 G. Mahmoudi, A. Bauzá and A. Frontera, *Dalton Trans.*, 2016, **45**, 4965–4969.

25 G. Mahmoudi, D. A. Safin, M. P. Mitoraj, M. Amini, M. Kubicki, T. Doert, F. Locherera and M. Fleck, *Inorg. Chem. Front.*, 2017, **4**, 171–182.

26 G. Mahmoudi, A. V. Gurbanov, S. Rodríguez-Hermida, R. Carballo, M. Amini, A. Bacchi, M. P. Mitoraj, F. Sagan, M. Kukułka and D. A. Safin, *Inorg. Chem.*, 2017, **56**(16), 9698–9709.

27 G. Mahmoudi, E. Zangrando, m. P. Mitoraj, A. V. Gurbanov, F. I. Zubkov, M. Moosavifar, I. A. Konyaeva, A. M. Kirillov and D. A. Safin, *New J. Chem.*, 2018, **42**, 4959–4971.

28 S. K. Seth, A. Bauzá, G. Mahmoudi, V. Stilinović, E. López-Torres, G. Zaragoza, A. D. Keramidas and A. Frontera, *CrystEngComm*, 2018, **20**, 5033–5044.

29 J. D. Velásquez, G. Mahmoudi, E. Zangrando, A. V. Gurbanov, F. I. Zubkov, Y. Zorlu, A. Masoudiasl and J. Echeverría, *CrystEngComm*, 2019, **21**, 6018–6025.

30 S. Mirdya, S. Roy, S. Chatterjee, A. Bauza, A. Frontera and S. Chattopadhyay, *Cryst. Growth Des.*, 2019, **19**, 5869–5881.

31 F. Akbari Afkhami, G. Mahmoudi, F. Qu, A. Gupta, E. Zangrando, A. Frontera and D. A. Safin, *Inorg. Chim. Acta*, 2020, **502**, 119350.

32 S. Mirdya, S. Banerjee and S. Chattopadhyay, *CrystEngComm*, 2020, **22**, 237–247.

33 F. Akbari Afkhami, G. Mahmoudi, F. Qu, A. Gupta, M. Kose, E. Zangrando, F. I. Zubkov, I. Alkorta and D. A. Safin, *CrystEngComm*, 2020, **22**, 2389–2396.

34 G. Mahmoudi, F. Akbari Afkhami, A. R. Kennedy, F. I. Zubkov, E. Zangrando, A. M. Kirillov, E. Molins, M. P. Mitoraj and D. A. Safin, *Dalton Trans.*, 2020, **49**, 11238–11248.

35 G. Mahmoudi, M. Abedi, S. E. Lawrence, E. Zangrando, M. G. Babashkina, A. Klein, A. Frontera and D. A. Safin, *Molecules*, 2020, **25**, 4056.

36 G. Mahmoudi, A. Masoudiasl, F. Akbari Afkhami, J. M. White, E. Zangrando, A. V. Gurbanov, A. Frontera and D. A. Safin, *J. Mol. Struct.*, 2021, **1234**, 130139.

37 I. García-Santos, A. Castiñeiras, G. Mahmoudi, M. G. Babashkina, E. Zangrando, R. M. Gomila, A. Frontera and D. A. Safin, *Inorg. Chim. Acta*, 2022, **538**, 120974.

38 G. Mahmoudi, I. García-Santos, M. Pittelkow, F. S. Kamounah, E. Zangrando, M. G. Babashkina, A. Frontera and D. A. Safin, *Acta Crystallogr., Sect. B: Struct. Sci., Cryst. Eng. Mater.*, 2022, **78**, 685–694.

39 I. García-Santos, A. Castiñeiras, G. Mahmoudi, M. G. Babashkina, E. Zangrando, R. M. Gomila, A. Frontera and D. A. Safin, *CrystEngComm*, 2022, **24**, 368–378.

40 D. Majumdar, A. Frontera, R. M. Gomila, S. Das and K. Bankura, *RSC Adv.*, 2022, **12**, 6352–6363.

41 G. Mahmoudi, E. Zangrando, A. V. Gurbanov, B. Eftekhari-Sis, M. P. Mitoraj, F. agan and D. A. Safin, *CrystEngComm*, 2023, **25**, 5100–5108.

42 A. Bauzá, T. J. Mooibroek and A. Frontera, *Angew. Chem., Int. Ed.*, 2003, **52**, 12317–12321.

43 I. Alkorta, J. Elguero and A. Frontera, *Crystals*, 2020, **10**, 180.

44 M. Servati Gargari, V. Stilinović, A. Bauzá, A. Frontera, P. McArdle, D. Van Derveer, S. W. Ng and G. Mahmoudi, *Chem. – Eur. J.*, 2015, **21**, 17951–17958.

45 P. Kumar, T. Firdoos, R. M. Gomila, A. Frontera and S. K. Pandey, *Cryst. Growth Des.*, 2023, **23**, 2138–2154.

46 (*a*) M. Karmakar, A. Frontera, S. Chattopadhyay, T. J. Mooibroek and A. Bauzá, *Int. J. Mol. Sci.*, 2020, **21**, 7091; (*b*) D. Majumdar, A. Frontera, S. Roy and D. Sutradhar, *ACS Omega*, 2024, **9**, 1786; (*c*) I. M. Garazade, A. V. Gurbanov, R. M. Gomila, A. Frontera, A. V. M. Nunes, K. T. Mahmudov and A. J. L. Pombeiro, *New J. Chem.*, 2023, **47**, 15856; (*d*) V. Alizadeh, G. Mahmoudi, E. Priola, S. K. Seth, J. M. White, A. Frontera and D. A. Safin, *Inorg. Chem. Commun.*, 2023, **149**, 110393.

47 (*a*) D. Dutta, P. Sharma, A. Frontera, A. Gogoi, A. K. Verma, D. Dutta, B. Sarma and M. K. Bhattacharyya, *New J. Chem.*, 2020, **44**, 20021–20038; (*b*) A. Das, P. Sharma, A. Frontera, A. K. Verma, M. Barcelo-Oliver, S. Hussain and M. K. Bhattacharyya, *J. Mol. Struct.*, 2021, **1223**, 129246.

48 T. Baishya, R. M. Gomila, A. Frontera, M. Barcelo-Oliver, A. K. Verma and M. K. Bhattacharyya, *Polyhedron*, 2023, **230**, 116243.

49 Bruker (2019), APEX3 Software, Bruker AXS Inc. v2019.11-0, Madison, Wisconsin, USA.

50 G. M. Sheldrick, SADABS, Program for Empirical Absorption Correction of Area Detector Data, University of Goettingen, Germany, 1997.

51 G. M. Sheldrick, *Acta Crystallogr., Sect. A: Found. Crystallogr.*, 2008, **64**, 112–122.

52 C. Adamo and V. Barone, *J. Chem. Phys.*, 1999, **110**, 6158–6170.

53 S. Grimme, J. Antony, S. Ehrlich and H. Krieg, *J. Chem. Phys.*, 2010, **132**, 154104–154118.

54 F. Weigend and R. Ahlrichs, *Phys. Chem. Chem. Phys.*, 2005, **7**, 3297–3305.

55 M. J. Frisch, G. W. Trucks, H. B. Schlegel, G. E. Scuseria, M. A. Robb, J. R. Cheeseman, G. Scalmani, V. Barone, G. A. Petersson, H. Nakatsuji, X. Li, M. Caricato, A. V. Marenich, J. Bloino, B. G. Janesko, R. Gomperts, B. Mennucci, H. P. Hratchian, J. V. Ortiz, A. F. Izmaylov, J. L. Sonnenberg, D. Williams-Young, F. Ding, F. Lipparini, F. Egidi, J. Goings, B. Peng, A. Petrone, T. Henderson, D. Ranasinghe, V. G. Zakrzewski, J. Gao, N. Rega, G. Zheng, W. Liang, M. Hada, M. Ehara, K. Toyota, R. Fukuda, J. Hasegawa, M. Ishida, T. Nakajima, Y. Honda, O. Kitao, H. Nakai, T. Vreven, K. Throssell, J. A. Montgomery, Jr., J. E. Peralta, F. Ogliaro, M. J. Bearpark, J. J. Heyd, E. N. Brothers, K. N. Kudin, V. N. Staroverov, T. A. Keith, R. Kobayashi, J. Normand, K. Raghavachari, A. P. Rendell, J. C. Burant, S. S. Iyengar, J. Tomasi, M. Cossi, J. M. Millam, M. Klene, C. Adamo, R. Cammi, J. W. Ochterski, R. L. Martin, K. Morokuma, O. Farkas, J. B. Foresman and D. J. Fox, *Gaussian 16, Revision C.01*, Gaussian, Inc., Wallingford CT, 2016.

56 S. F. Boys and F. Bernardi, *Mol. Phys.*, 1970, **19**, 553–566.

57 R. F. W. Bader, *Chem. Rev.*, 1991, **91**, 893–928.

58 J. Contreras-Garcia, E. R. Johnson, S. Keinan, R. Chaudret, J.-P. Piquemal, D. N. Beratan and W. Yang, *J. Chem. Theory Comput.*, 2011, **7**, 625–632.

59 T. A. Keith, *AIMAll (Version 13.05.06)*, TK Gristmill Software, Overland Park, KS, 2013.